# Visualising mineralisation processes and fossil anatomy using synchronous synchrotron X-ray fluorescence and X-ray diffraction mapping

**Pierre Gueriau[1,2,3], Solenn Réguer[1], Nicolas Leclercq[1], Camila Cupello[4], Paulo M. Brito[4], Clément Jauvion[5,6], Séverin Morel[6], Sylvain Charbonnier[6], Dominique Thiaudière[1], Cristian Mocuta[1]**

*[1]Synchrotron SOLEIL, L'orme des Merisiers, Saint-Aubin BP 48, F-91192 Gif-sur-Yvette Cedex, France*

*[2]Université Paris-Saclay, CNRS, ministère de la Culture, UVSQ, MNHN, Institut photonique d'analyse non-destructive européen des matériaux anciens, F-91192, Saint-Aubin, France.*

*[3]Institute of Earth Sciences, University of Lausanne, Géopolis, CH-1015 Lausanne, Switzerland*

*[4]Departamento de Zoologia, Instituto de Biologia/IBRAG, Universidade do Estado do Rio de Janeiro, R. São Francisco Xavier, 524-Maracanã, Rio de Janeiro 20550–900, Brazil*

*[5]Muséum national d'Histoire naturelle, Sorbonne Université, CNRS UMR 7590, IRD, Institut de Minéralogie, de Physique des Matériaux et de Cosmochimie, IMPMC, F-75005 Paris, France*

*[6]Centre de Recherche en Paléontologie – Paris (CR2P UMR 7207), CNRS, Sorbonne Université, Muséum National d'Histoire Naturelle, 57 rue Cuvier, CP38, F-75005 Paris, France*

*Authors for correspondence:

Pierre Gueriau; email: pierre.gueriau@hotmail.fr

Cristian Mocuta; email: cristian.mocuta@synchrotron-soleil.fr

ORCID

PG, 0000-0002-7529-3456

CC, 0000-0001-6030-8670

PMB, 0000-0002-4853-8630

CJ, 0000-0002-3245-8222

CM, 0000-0001-5540-449X

**Fossils, including those that occasionally preserve decay-prone soft-tissues, are mostly made of minerals. Accessing their chemical composition provides unique insight into their past biology and/or the mechanisms by which they preserve, leading to a series of developments in chemical and elemental imaging. However, the mineral composition of fossils, particularly where soft-tissues are preserved, is often only inferred indirectly from elemental data, while X-ray diffraction that specifically provides phase identification received little attention. Here, we show the use of synchrotron radiation to generate not only X-ray fluorescence elemental maps of a fossil, but also mineralogical maps in transmission geometry using a two-dimensional area detector placed behind the fossil. This innovative approach was applied to millimetre-thick cross-sections prepared through three-dimensionally preserved fossils, as well as to compressed fossils. It identifies and maps mineral phases and their distribution at the microscale over centimetre-sized areas, benefitting from the elemental information collected synchronously, and further informs on texture (preferential orientation), crystallites size and local strain. Probing such crystallographic information is instrumental in defining mineralisation sequences, reconstructing the fossilisation environment, and constraining preservation biases. Similarly, this approach could potentially provide new knowledge on other (bio)mineralisation processes in environmental sciences. We also illustrate that mineralogical contrasts between fossil tissues and/or the encasing sedimentary matrix can be used to visualise hidden anatomies in fossils.**

**Keywords**

(bio)mineralisation, mineral/life interactions, exceptional fossilisation, synchrotron imaging

## 1. Introduction

Fossils mostly consist of the mineralised remains or impressions of organisms. Biomineralised tissues such as invertebrate shells or vertebrate bones and teeth, which are highly resistant to decay, form the bulk of the fossil record (note that they usually undergo physico-chemically changes during fossilisation). Occasionally, decay-prone soft parts (e.g. muscles, nervous systems) or even entire soft-bodied organisms such as worms, jellyfish or squid are 'exceptionally' preserved, offering us a more detailed view into the past than skeletal remains alone. Nonetheless, soft-tissues rarely survive as organic components. Instead, their preservation results from poorly constrained mineralisation processes such as the permeation of tissues by mineralising fluids (permineralisation) or the rapid in-situ growth of minerals (authigenic mineralisation) driven by the activity of bacterial decay [1]. Better constraining these taphonomic processes is critical for circumventing any potential fossilisation bias (e.g. size, taxonomic or tissue sorting that affects exceptional preservation deposits [1,2]), and properly interpret these invaluable snapshots of past life.

The mineralogical characterisation of such exceptionally preserved fossils was historically assessed through petrographic observations of thin sections, later complemented –or even replaced– by the use and/or development of the most cutting-edge techniques available. As a result, the mineralogical composition of a fossil is nowadays largely inferred indirectly from its elemental composition, usually obtained from scanning electron microscope (SEM) energy-dispersive X-ray spectroscopy and mapping (e.g. [3]) or laser ablation (LA) ICP-MS (e.g. [4]). More recently, improvement in synchrotron rapid scanning (SRS) X-ray fluorescence (XRF), which produces 2D distributions of major-to-trace elements for decimetre-scale objects, offers additional palaeobiological, palaeoenvironmental and taphonomic information [5–11].

In contrast, X-ray diffraction (XRD), which specifically identifies the minerals present is rarely used by palaeontologists as it requires destructive sampling and powder preparation, and often only provides limited spatial information in highly heterogeneous materials such as fossils. In few studies, electron backscatter diffraction (EBSD), a SEM–based technique that provides information about the structure, crystal orientation (texture), phase or strain in materials (e.g. [12]), was used to disentangle mineralisation processes in fossils. For instance, it revealed key insight into biological control of mineral formation in mollusks, brachiopods and trilobites [13] but also microfossils [14]. Nevertheless, EBSD is restricted to sample sizes accommodated by the SEM chamber, operates mostly in reflection such that it requires the preparation of a finely polished sample surface, and the electron beam only diffracts in the first few lattice layers (typically ~50 nm). Extracting information not restricted to the very surface (i.e. from the volume or bulk) can be achieved in transmission geometry, using a detector placed behind the sample. This requires high-energy X-ray beams adapted to the thickness of the material under investigation, and has been particularly used for the visualisation of paintings hidden underneath layers containing heavy elements that prevent the use of XRF mapping (e.g. [15]). As for palaeontology, Mürer et al. [16] non-destructively reconstructed 3D maps of mineral composition and hydroxyapatite orientation in small (1–2 cm) bones of early tetrapod and lobe-finned fish by combining XRD and CT using very high-energy X-rays (86.6 keV) within a 12–72-hour time frame acquisition. Lower X-ray energies of 6–30 keV (commonly available at XRD synchrotron beamlines) enable imaging in 2D the mineralogical structure and microtexture of thinner samples or sections, e.g., of modern and archeological otoliths, within a reasonable time frame (typically ~10 minutes for 32 kilopixel images, i.e. ~5 hours for megapixels images) and coupled to XRF mapping [17].

Here we assess the potential of XRD mapping for investigating mineralisation processes in the fossil record, using four fossils representing a wide range of (i) taxonomic affinities (arthropods, sarcopterygians and actinopterygians), (ii) types of preservation (compressed and 3D fossils, including extensive soft-tissue mineralisation) and (iii) ages and depositional environments. We produce megapixel mineralogical maps across millimetre thick cross-sections through 3D-preserved fossils and pluri-centimetre compressed fossils (up to $5 \times 3$ $cm^2$ lateral area). Insights into mineral identification and distribution at the microscale over large areas, as well as crystallite orientation and size in fossils show great promise for taphonomic and anatomical studies.

## 2. Material and methods

Mineralogical maps were collected synchronously with X-ray fluorescence maps at the DiffAbs beamline of the SOLEIL synchrotron source (France), owing to the development of a fast and multi-technique data acquisition platform at the SOLEIL synchrotron (the FLYSCAN platform [18]).

### 2.1. Experimental setup

Synchronous synchrotron rapid scanning X-ray fluorescence and diffraction mapping (SRS-XRFD) was performed using an incident X-ray beam of 16.2 or 18 keV, monochromatised using a Si(111) double-crystal monochromator, with a beam size diameter reduced down to 50 or 100 µm using platinum pinholes, or focused down to ~10 µm using Kirkpatrick-Baez mirrors [19].

122 XRF was collected using a 4-element silicon drift detector (SDD, Vortex ME4, Hitachi High-
123 Technologies Science America, Inc., total active area: 170 $mm^2$) oriented at 90° to the incident
124 beam, in the horizontal plane. XRD was collected in transmission geometry using a 2D hybrid
125 pixel detector (XPAD S140, 240×560 pixels of 130 μm each [20–23]), which is placed behind
126 the sample at a distance of typically 200–300 mm such to intercept diffraction rings over an
127 angular range of ~7° in scattering angle (2θ). Several images can be collected along the 2θ angle
128 by moving the detector in order to extend the available 2θ domain; one can also settle for a single
129 detector position using *a priori* knowledge of the fossil composition to select a 2θ domain
130 encompassing the diffraction peaks of interest (note that larger detectors can be used to cover a
131 wider domain; e.g. [15,16]). Details about detector design, geometry, calibration, correction of
132 the images, and diagram (or profile) reconstructions from the corrected images are available in
133 [23, 24] and references therein. Figure 1*a* shows a schematic view of the setup.
134 Two-dimensional scanning was done by moving laterally the fossils in a plane rotated
135 around the vertical axis by 20° to the primary beam (i.e., incident angle), to limit X-ray beam
136 footprint on the sample but also such that the sample exhibits its surface to the SDD detector (no
137 shadowing of the reflected XRD signal, figure 1*a*). Mapping over the entire fossils at a 35–100
138 μm lateral resolution was performed on the fly using the FLYSCAN platform [18]. A full XRF
139 spectrum and one or several XRD images were collected at each pixel.
140
141 **2.2. Data processing**
142 ***2.2.1. Images generation and phase identification***
143 XRD images were processed through self-written routines (azimuthal data regrouping along ψ
144 direction) to extract their respective diffractograms (Intensity *vs.* 2θ profiles), and generate 4D

datasets (x, y, 2θ, intensity) and then particular XRD contrast maps. Phase identification and 2θ calibration were performed using powder XRD diffractograms obtained on fragments of the sedimentary matrix (and of the fossil when possible) using the Match! software (Crystal Impact) making use of the International Centre for Diffraction Data (ICDD)- PDF 2015 database. Additional peaks in the XRD maps could then be identified using Match/ICDD database, as well as from the elemental information provided by the XRF data. All mineralogical and elemental distributions presented herein correspond to integrated intensities from the main XRD and XRF peaks, represented using linear (expect figure 1*b*, logarithmic) grey or colour scales that go from dark to light, respectively for low to high intensities. By Gaussian fitting the 2θ profile of XRD peaks attributed to different crystalline phases, corresponding crystallite sizes were extracted (for each pixel of the maps) by converting their full width at half maximum (FWHM) using Scherrer's formula. It was assumed that only the crystallite size is contributing to the broadening, and an instrument resolution function measured as ~0.035° (amounting several 10 %, and up to 50 % of the measured peak FWHM) was also taken into account for FWHM deconvolution.

***2.2.2. Local texture measurements***

In order to confirm some microstructure results obtained using the local probe XRD approach, supplementary local texture measurements were performed on a 'rod'-shaped sample (~24 × 1.5 × 1.5 $mm^3$ H×W×L) extracted using a diamond wire saw (figures 2*a*, 3*a*).

A texture measurement allows retrieving information about the orientation of the crystallites in the sample: for a fixed 2θ position of the detector (i.e. accessing a particular inter-reticular distance), the sample is oriented in all positions in the angular space. This is done by scanning it in azimuth (φ, rotation around the sample surface normal) and elevation (ψ, rotation

around the projection of the impinging X-ray beam on the sample surface), while recording, at each position, the X-ray scattered signal. The resulting intensity is represented in a map, in polar coordinates (azimuth angle and elevation, e.g. figures 3*f–h*). In this way, when one or several crystallites are oriented such that the Bragg law is fulfilled for the particular inter-reticular distance probed (or the particular Bragg angle 2θ), high signal is found in the particular corresponding regions of the polar map, allowing: i) to retrieve the particular orientation of the grains (φ, ψ), and ii) to possibly quantify the volume ratio of that particular orientation, compared to other orientations on the map.

Rapid texture measurements were performed using the area detector (XPAD). The sample was illuminated by the impinging X-ray beam (of size ~ 150 × 150 μm$^2$ in this case) and the azimuth (φ) and elevation (ψ) angles were scanned, the first one continuously. An image was recorded in each φψ point, then texture maps for various 2θ angles (i.e. volumes) were reconstructed [24]. Then, a similar dataset was recorded at the next vertical position on the sample. A rod-shaped sample is required in this case due to the azimuthal rotations during the measurements: as for the transmission XRD experiment, the sample dimension along the transmitted beam path needs to be relatively small (~ 1.5 × 1.5 mm$^2$ in this case). This approach is expected to give volume texture information with a lateral resolution of about 150 – 200 μm along the sample long dimension.

### 2.3. Samples

The potential of this approach is illustrated using four fossils from different localities representing a wide range of taxa (an arthropod, a sarcopterygian and two actinopterygians), ages (Mesozoic and Cenozoic), sedimentary environments (concretions, shale, limestone),

preservation types (compressed and 3D, including extensive soft-tissue mineralisation) and mineralogical compositions (carbonates, phosphates, metal sulfides and oxides). 3D fossils of the arthropod *Dollocaris ingens* Van Straelen, 1923, and the superimposed lung plates of the coelacanth *Axelrodichthys araripensis* Maisey, 1986 were prepared as millimetre-thick cross-sections using a diamond disk saw. For *A. araripensis*, the fossil was embedded in resin, and we additionally extracted a 'rod-shaped sample' (mentioned above), so that 5 samples have actually been studied herein. Compressed specimens of the osteoglossomorph *Laeliichthys ancestralis* Santos, 1985, and of the cyprinodontiform *Prolebias goreti* Sauvage, 1878, were thin enough for X-ray transmission and were therefore mapped without any preparation. Age, locality, accession number, preservation, sedimentology and sample preparation information are available in table 1.

## 3. Results and discussion

### 3.1. Identification and distribution of minerals at the microscale

XRD mapping successfully produce contrasts, with peak positions and intensities varying depending on the sample composition (figure 1). Nonetheless, unlike in rotating powder XRD, only polycrystalline materials can here display all peaks (orientations); not all the crystalline planes being in position to diffract the incident beam in non-polycrystalline phases. This can be seen by the rather 'speckle' feature of the XRD rings (figure 1*c*). Quantitative phase analyses (using Rietveld refinement) therefore can usually not be performed here, yet SRS-XRFD allows fine phase identification (figure 1*d*; constrained by XRF collected synchronously, and additional powder XRD diffractograms collected on the sedimentary matrix surrounding the fossil, or

214 fragments of the fossil itself when possible), and offers the capability to image their distribution
215 with <100µm lateral resolution over centimetric lateral sized samples (figure 1*e*).
216 Figure 1 shows 100-kilopixel mineralogical maps collected from a millimetre-
217 thick transversal section of the thylacocephalan arthropod *Dollocaris ingens* (specimen
218 MNHN.F.A66910), clearly displaying the heart, muscles and gills preserved (figure 1*a,b*). This
219 fossil, as well as most others from the deep-water ecosystem of La Voulte [25,26], exhibits a
220 unique preservation style where most labile soft-tissues are three-dimensionally retained in a
221 complex mineral association including sulfides [27], providing pivotal information about the
222 affinities and lifestyle of several fossil groups including thylacocephalans [28]. Wilby et al. [27]
223 proposed a taphonomic scenario, including a diagenetic sequence of mineral precipitation, where
224 apatite served as 'a template for calcification and pyritisation'. Nonetheless. many details of the
225 anatomy of these fossils have been lost, indicating that there are unidentified fossilisation biases.
226 In this context, Jauvion et al. used SRS-XRFD in combination with optical and electronic
227 microscopies, EDX, powder XRD, and speciation X-ray absorption spectroscopy, to investigate
228 fossilisation biases in the abundant *D. ingens* [29]. Indirect (SEM-EDX, XRF) and direct (XRD)
229 mineralogical characterisation allowed the authors to identify and locate the various phases
230 comprising the fossils, showing that histologically similar tissues were replaced by the same
231 minerals under fast biodegradation [29].
232 XRD precisely identified that cuticle and muscle fibres are preserved in fluorapatite, and
233 epithelia-rich tissues (gills, digestive gland) in pyrite and pyrrhotite [29], Arsenopyrite is also
234 present in muscle, as well as in the appendages, where they underlie muscular structures (figure
235 1*e*, blue). Calcite is observed in the external part of the heart, but also where no organ is
236 morphologically preserved and in the surrounding matrix (figure 1*e*, green). Dolomite is only

found in the centre of the heart (figure 1*e*, red). Contrasting with the scenario proposed by Wilby et al. [27], data from MNHN.F.A66910 and several other specimens rather suggest that sulfide minerals and apatite precipitated concomitantly [29].

From a taphonomic point of view, localising the different phases at the microscale over the entire organism (or here cross-section) is instrumental in defining a taphonomic sequence. Moreover, pinpointing tissue-specific mineralisation processes is crucial for understanding taphonomic biases. The fact that different tissue types are replicated in a certain mineral emphasizes that fossilisation processes are not homogeneous across the whole fossil, hence, a lack of favourable conditions for these minerals to precipitate might result in the loss of a whole group of tissues. Last but not least, identifying the precise mineralogical nature of phases has allowed Jauvion et al. [29] to better constrain precipitation-favourable physico-chemical parameters, and therefore reconstitute the fossilisation environment.

### 3.2. Additional taphonomic information embedded in the XRD images

Besides crystalline phase identification and their spatial distribution, the XRD data also contain information about the material structure and microstructure (figure 2). This is particularly interesting for mapping over pluri-centimetric areas, as shown herein, as the incident beam spot size used is much larger than the size of the crystallites constituting the fossil and its surrounding sedimentary matrix. In this case, XRD images acquired by the area detector can show i) continuous rings (though sometimes slight speckle-like features are clearly visible), which result from diffraction of powder-like polycrystalline phases (*i.e.* random oriented small crystallites), ii) ring segments that evidence texture (preferential crystalline orientation), and iii)

spots (disposed on the corresponding ring) that indicate isolated grains (figure 2*e*). In turn, would the beam size be of similar size or smaller than the crystallites (i.e. when using micrometre or nanometre beams for very high-resolution analyses) only spots will potentially appear on the XRD images, if and only if the illuminated crystallite is in the right geometrical orientation to fulfill diffraction condition. In addition, the peak width is depending on the corresponding crystallites sizes (inversely proportional, i.e., the smaller the crystallites the wider the diffraction peaks [30]) and the local / micro-strain. In the absence of the latter the width of the diffraction peaks can therefore be converted to crystallite sizes (along a direction which can be retrieved from the geometry of the experiment), allowing to produce maps using crystallites size as a contrast signal (figure 2*g*).

Such results are illustrated against a millimetre-thick transversal section through superimposed lung plates of the coelacanth *Axelrodichthys araripensis* (specimen UERJ-PMB 143) from the ~110-million-year old Santana Formation of the Araripe Basin, Brazil (figure 2*a*). A peculiarity of coelacanths is indeed the presence of a lung covered by ossified plates, described for almost all coelacanth taxa ranging from the Palaeozoic to the Recent [31–34]. Enriched in yttrium (figure 2*b*), suggesting an apatite composition [35], these plates are confirmed to be of apatitic bone nature by SRS-XRFD (figure 2*c*,*f*), as previously recognised from the observation of cellular bone with star-shaped osteocytes and a globular mineralisation [33]. While hardly visible on the optical photograph, elemental and mineralogical maps further show that inner lung plates (i.e. the lowest plates in figure 2*a–c*, closer to the lung) are thinner than outer plates, confirming previous observations on ground cross-thin sections [31,36], and suggests that, most probably, these superimposed elements are formed first from the region closest to the lung surface than the outermost region. Note that the section has been prepared

transversally through a crushed lung (see [31], text-fig 2D) and as such the cutting plane had little geometric impact on the plate thickness. The plates cover a calcium-rich area (figure 2*b*) made of large grains of calcite (figure 2*c,d*) exhibiting important texture (figure 2*d,e*) evidencing an infilling of the void created by lung decay. The surrounding carbonate concretion includes clay and quartz minerals (figure 2*b,c*).

Apatite peaks from the lung plates are much wider than calcite and quartz peaks (figure 2*f*), indicating that the plate crystallites are much smaller than those in the lung infill and the concretion. Crystallites size extraction show that apatite crystallites from the lung plates yield a homogeneous size of ~10–15 nm, whereas calcite and quartz crystallites are an order of magnitude larger and less uniform in size (~50–150 nm) (figure 2*g*). This data is totally in accordance with the homogeneity of the ossified, compacted and dense lung plates composed by true cellular bone tissue with osteocytes and globular mineralisation, separated by layers of coarser limestone matrix, observed in thin sections [31,33]. Lung plates of adult specimens of *A. araripensis* are constituted only by thin layers of homogeneous and compact bone tissue, contrasting to other coelacanth taxa (such as *Swenzia latimeriae* Clément, 2005) that may display, in addition, a non-mineralised region composed of a collagenic packet of microfibrils [33].

In view of the large inhomogeneities observed in crystallites size maps at different sample locations (figure 2*g*, see e.g. missing information in areas shown as dark background), the data highlight the existence of a significant, and variable, crystallites orientation, which is far from being that of a randomly oriented powder. Indeed, extended 2D diffractograms at particular points in the sample (figure 2*e*) show, as mentioned before, the presence of XRD segments instead of isotropic rings. For highly textured samples, performing XRD measurements at fixed

sample geometry could result into missed crystallinity information: crystallites corresponding to a particular phase are never in diffraction condition, thus no XRD corresponding peaks are detected. In order to illustrate this issue, a first XRD experiment was performed on the aforementioned rod-shaped sample (figure 3*a*): the sample was scanned along the vertical direction (z), at fixed azimuth and elevation angles (φ, ψ), and, in each point, XRD datasets were recorded (figure 3*b,c*). One can already note that, for the 2 shown measurements, the diffractograms for 2 azimuths exhibit presence / absence of some XRD peaks at particular z-coordinates (see e.g. the domain highlighted by circles in figure 3*b,c*). Thus, such a simple measurement does not ensure accessing all the characteristic XRD peaks and potentially might miss some of them. To overcome this issue, texture measurements were performed at each z position. A first way to exploit the texture datasets consists in extracting, for each z sample position, the XRD signal as the summation of all the corresponding XPAD images (azimuths & elevations angles). This approach ensures that all crystallites are brought into diffraction condition and potentially diffract, and it is now expected to obtain, from our illuminated volume ($\sim 0.15 \times 1.5 \times 1.5$ mm$^3$), a diffractogram corresponding to that of a random powder (figure 3*d*). The most striking differences are the presence, in the aforementioned texture map, of XRD peaks in the z-range 5–9 mm (calcite void-infilling of the lung cavity) for 2θ values around 14° and 18° (unbroken ellipses in figure 3*b–d*); they were completely missing in all the tested fixed azimuth (0 to 80° range, every 20°) and fixed elevation (0°) configurations (line scans). Surprisingly, some apatite appears also associated to calcite in this region (dotted ellipses in figure 3*b–d*), likely to represent fragments of ossified plates that collapsed in the void left by the decay of the lung, or possibly phosphatised remains of the lung or soft-tissues, common in the Santana Formation [37,38].

Full data exploitation of texture measurements is achieved through the generation of pole figure volumes (5D datasets, φ, ψ, 2θ, z, Intensity). At particular 2θ scattering angles characteristic of the crystalline phases of interest (see figure 2*f*), pole figures at each z-coordinate are extracted (e.g. figure 3*f–h*). The result is shown as a volume in figure 3*e*, in which pole figures along the z-direction and for particular 2θ angles (and thus different crystalline structures) are shown as 3D iso-surfaces. This clearly demonstrates that missing information in areas such as the calcite void-infilling of the lung cavity that arose as dark background in figure 2*g* (z-range 5–9 mm in figure 3) results from an absence of diffraction in the used geometry (see how XRD peaks are not missed anymore in the pole figure volume figure 3*e–h*). This 3D visualisation further reveals a layered structure of the sample, particularly visible for the calcite void-infilling of the lung cavity. Several other regions in the sample deserve a closer look. Around z ~ 13 mm, crystallites orientation is much more pronounced, as seen by the presence of localised scattered signal ('hot spots') in the particular polar maps (figure 3*f–h*). In the case of the calcite void-infilling, the signal is much more diffuse and its position slowly rotates in φ and ψ, as illustrated in the 3D view (blue surface figure 3*e*). The crystallites of all the phases identified can rotate with large amplitudes of several 10°, having variable preferential orientation, for different z positions on the sample. This is illustrated by the 2 pole figures extracted for the apatite (taken 5 mm apart): the scattered intensity is grouped (within 10–20°) around (φ ~ 45° / ψ ~ 10, 40 and 90°) and (φ ~ 0° / ψ ~ 75° and φ ~ 90° / ψ ~ 20°) respectively (figure 3*h*).

Although this clearly shows the potential limitations of XRD mapping performed at fixed sample angles, one has to keep in mind not only the much longer time needed to perform such data acquisitions, but also the particular (rod-shaped) sample preparation required. *Sensu stricto*,

352 the hypothesis of perfectly random-oriented polycrystalline phases does not hold. Yet, in the case
353 of samples such as the fossils investigated herein, crystallites orientation still spans over several
354 10°, ensuring that the various crystalline phases (and related information such as the average
355 crystallite size, see above) can be detected (though possibly only partially) even for fixed sample
356 angular positions.

357 Considering now the above remarks, we can assume that texture is also visible in the
358 mineralised heart of the 3D-preserved thylacocephalan MNHN.F.A66910 (figures 1*e*, 4): speckly
359 regions of the calcite and dolomite maps are probably characteristic of large size grains, possibly
360 with specific orientations. Elongated crystals of calcite with alternating, ordered orientation grew
361 at the periphery of the heart, while the centre has been replaced with much poorly organised
362 dolomite (figures 1*e*, 4). This reveals a two-steps sequence of mineralisation within the heart,
363 contrary to the supposed coprecipitation with calcite in Jauvion et al. [29], which was tested
364 possible with geochemical modelling. Moreover, the same model suggests calcite dissolution and
365 dolomite precipitation while a later oxidation event is taking place, which might have been the
366 case locally.

367 From a taphonomic point of view, the latter example shows how crystallographic data
368 offer important information complementary to phase identification in the reconstruction of
369 mineralisation sequences. More generally, assessment of the distributions of crystallite size and
370 orientation, in particular preferential orientations (or misorientations) in non-isotropic materials,
371 is crucial for both palaeontological and taphonomic studies as they provide unique information
372 for deciphering the mineralisation processes associated with biomineralisation, fossilisation
373 and/or diagenesis. We should also point out here that variations in the position of a diffraction
374 peak (in 2θ) can be due to a modification of intereticular distances, and thus highlight strain

(thermal or mechanical) undergone by the materials during burial or diagenesis. Moreover, resolving crystallographic parameters in the skeleton of problematic extinct microorganisms has been shown (using EBSD in that case) to help in the determination of their affinities [14], and could also be used for larger organisms and/or their tissues.

### 3.3. Mineralogical contrasts reveal hidden anatomies

The mineralogical contrasts offered by SRS-XRFD can also be exploited to image compressed fossils that remain difficult (or impossible) to describe using conventional imaging methods such as optical photography and microscopy. We applied SRS-XRFD to two compressed fossil fishes (figure 5), generating up to 1.2-megapixel maps for a specimen of the osteoglossomorph *Laeliichthys ancestralis* (specimen 099-PV-DZ-UERJ) from the ~125-million-year old Sanfransiscana Basin, Brazil (figure 5*a,b*). The distribution of fluorapatite from their skeleton allows for the visualisation of their anatomy (figure 5*b,e*), with a resolution sufficient to observe tiny details such as central hollow tubes within the ribs of *Laeliichthys* (figure 5*c*). In the case of a specimen of the cyprinodontiform *Prolebias goreti* (specimen MNHN.F.CRT255) from the ~30-million-year old Apt-Céreste-Forcalquier Basin, southern France, hidden within a thin slab of limestone (figure 5*d*), fluorapatite maps even offer a way better contrast (figure 5*e*) than XRF mapping of yttrium (figure 5*f*), an element that preferentially substitutes for calcium in calcium phosphates such as bone apatite, and has been shown to yield useful anatomical contrasts for a wide range of fossils [35]. With an information depth of one to a few millimetres (depending on the energy of the X-ray used and the density of the material), SRS-XRFD mineralogical mapping of fossil slabs that thin therefore appears as a promising complement to SRS-XRF elemental

mapping, which only gives access, in most fossils, to the first 100 µm at the surface of the sample (see [35]), to reveal hidden anatomies in compressed fossils. Texture can also provide interesting anatomical contrasts, distinguishing, for instance, between different bones, and scales in *Laeliichthys* (figure 5*b*).

## 4. Potential limitations

There are three main inherent limitations to SRS-XRFD 2D mapping: (1) the illuminated crystallites need to be in the right geometrical orientation to diffract; (2) the beam spot size should be larger than the size of the crystallites to obtain continuous rings (pending that condition (1) is fulfilled; if the beam size is of similar size or smaller than the crystallites, e.g. for high lateral resolution analyses, only spots will possibly appear on the XRD images); and most importantly (3) as the approach works in transmission geometry samples have to be thin enough to allow transmission. Conditions (1) and (2) are discussed and illustrated in §3.2 (note that because of condition (1) quantitative phase analyses cannot usually be performed here). Regarding condition (3), maximum sample thickness for a given material depends on the X-ray energy used (the higher the energy, the more X-rays penetrate). Within the 6–30 keV range of energies commonly available at XRD synchrotron beamlines, X-rays can probe up to a few millimetre-thick fossils (depending on the exact photon energy used and the density of the material), such that SRS-XRFD is well-adapted to millimetre-thick cross-sections prepared through three-dimensionally preserved fossils, but also to compressed fossils on slab that thin. It works also with thin sections, though they must be uncovered in order to take advantage of XRF collected synchronously in reflection geometry (the underlying glass slide on which they are

mounted is not problematic as it does not produce a sharp diffraction that competes with that of the sample). Nonetheless, finely polished sections (30 μm or below) may not present a sufficient diffracting volume, resulting in a poor signal (or require increased exposure times per point for reasonable statistics); preference should therefore be given to sections polished to 100 μm or thicker (not thicker than a few millimetres to allow X-ray transmission; see above).

## 5. Conclusion

In this paper, we introduce synchrotron rapid scanning transmission X-ray diffraction, synchronously coupled to X-ray fluorescence mapping (SRS-XRFD), as a novel method of identifying and mapping minerals at the microscale over pluri-centimetric thin fossils and sections, within a reasonable time frame and with bulk sensitivity. XRF major-to-trace elemental mapping helps phase identification, and informs on trace element incorporations within minerals. Besides phase identification and corresponding lateral distribution in the sample, SRS-XRFD further informs on texture (preferential orientation), crystallites size and local strain, providing unique information to characterize fossil tissues and decipher fossilisation processes (figures 1–4). In the examples presented herein, we particularly highlight how pinpointing tissue-specific phase distributions and crystallographic characteristics is instrumental in defining mineralisation sequences, reconstructing the fossilisation environment, and constraining preservation biases. In addition, this approach offers at least three other promising perspectives for taphonomic and palaeontological research: (1) the ability to similarly characterise both 3D fossils (using cross-sections) and entire compressed fossils, which is hardly possible through the petrographic observation of thin sections, provide a unique way to compare preservation mechanisms at stake

444 in formations that yielded both 3D and compressed fossils; (2) SRS-XRFD could be applied to
445 fossils of the earliest known chordates and vertebrates with the aim to detect the first signs of
446 hydroxyapatite biomineralisation (bone) in the fossil record, and to understand how the first
447 forms of bone have evolved, how they were constructed, and their potential functions; (3) used in
448 an integrative way, tissue-specific mineralisation identified at the locality level could reveal the
449 affinities of enigmatic tissues and/or organisms. Mapping mineral distributions and
450 crystallographic parameters at the microscale could also potentially provide new insight into
451 other (bio)mineralisation processes in environmental sciences. Finally, we show that tissue-
452 specific mineralogical compositions, and/or differences with the encasing sedimentary matrix,
453 can represent a new source of contrasts to visualise hidden anatomies in compressed fossils for
454 which X-ray tomography is limited, and/or which are buried too deeply within the sediment for
455 SRS-XRF mapping (figure 5).
456
457 **Data accessibility**. All data used in this work are publicly available via the following Dryad Digital
458 Repository: Gueriau P, Réguer S, Leclercq N, Cupello C, Brito PM, Jauvion C, Morel S,
459 Charbonnier S, Thiaudière D, Mocuta C. 2020 Data from: Visualising mineralisation processes
460 and fossil anatomy using synchronous synchrotron X-ray fluorescence and X-ray diffraction
461 mapping. Dryad Digital Repository. https://doi.org/10.5061/dryad.s7h44j13z.
462
463 **Authors' contributions.** C.M., S.R., D.T. and N.L. implemented the setup on the beamline.
464 C.M. developed data processing routines. P.G. and C.M. conceived the study, performed the
465 experiments and processed and interpreted the data. C.C., P.M.B, C.J., S.M and S.C. provided

the samples and helped with data interpretation. P.G., S.R. and C.M. drafted the manuscript. All authors contributed to the final editing.

**Funding.** This research has been supported by SOLEIL synchrotron. CC was funded by the Coordenação de Aperfeiçoamento de Pessoal de Nível Superior – Brasil (CAPES) – Finance Code 001 (Programa Nacional de Pós Doutorado-PNPD) and Programa de Apoio à Docência – UERJ.

**Acknowledgements.** We are grateful to SOLEIL synchrotron for provision of beamtime, P. Joly for assistance at the DiffAbs beamline, S. Blanchandin and K. Chaouchi for their help with X-ray powder diffraction, as well as J. Berthauld and teams at the Control & data acquisition 'software and IT' and 'Electronic systems' groups of SOLEIL synchrotron for the development of the FLYSCAN platform. C. Fossé prepared the rod-shaped sample. The authors also warmly thank A. Daley for English edits, and the reviewers, whose comments, suggestions and corrections helped to improve the manuscript.

## References

1. Briggs DEG. 2003 The role of decay and mineralization in the preservation of soft-bodied fossils. *Annual Review of Earth and Planetary Sciences* **31**, 275–301. (doi:10.1146/annurev.earth.31.100901.144746)
2. Wilson P, Parry LA, Vinther J, Edgecombe GD. 2016 Unveiling biases in soft-tissue phosphatization: extensive preservation of musculature in the Cretaceous (Cenomanian)

polychaete *Rollinschaeta myoplena* (Annelida: Amphinomidae). *Palaeontology*, **59**, 463–479. (doi:10.1111/pala.12237)

3. Orr PJ, Briggs DEG, Kearns SL. 1998 Cambrian Burgess Shale animals replicated in clay minerals. *Science* **281**, 1173–1175. (doi:10.1126/science.281.5380.1173)
4. Koenig AE, Rogers RR, Trueman CN. 2009 Visualizing fossilization using laser ablation–inductively coupled plasma–mass spectrometry maps of trace elements in Late Cretaceous bones. *Geology* **37**, 511–514. (doi:10.1130/G25551A.1)
5. Bergmann U, Morton RW, Manning PL, Sellers WI, Farrar S, Huntley KG, Wogelius RA, Larson PL. 2010 *Archaeopteryx* feathers and bone chemistry fully revealed via synchrotron imaging. *Proceedings of the National Academy of Sciences, USA* **107**, 9060–9065. (doi:10.1073/pnas.1001569107)
6. Bergmann U, Manning PL, Wogelius RA. 2012 Chemical mapping of paleontological and archeological artifacts with synchrotron X-rays. *Annual Review of Analytical Chemistry* **5**, 361–389. (doi:10.1146/annurev-anchem-062011-143019)
7. Wogelius RA, Manning PL, Barden HE, Edwards NP, Webb SM, Sellers WI, Taylor KG, Larson PL, Dodson P, You H, Da-qing L, Bergmann U. 2011 Trace metals as biomarkers for eumelanin pigment in the fossil record. *Science* **333**, 1622–1626. (doi:10.1126/science.1205748)
8. Anné J, Edwards NP, Wogelius RA, Tumarkin-Deratzian AR, Sellers WI, van Veelen A, Bergmann U, Sokaras D, Alonso-Mori R, Ignatyev K, Egerton VM, Manning PL. 2014 Synchrotron imaging reveals bone healing and remodelling strategies in extinct and extant vertebrates. *Journal of the Royal Society Interface* **11**, 20140277. (doi:10.1098/rsif.2014.0277)

9. Gueriau P, Mocuta M, Dutheil DB, Cohen SX, Thiaudière D, The OT1 Consortium, Charbonnier S, Clément G, Bertrand L. 2014 Trace elemental imaging of rare earth elements discriminates tissues at microscale in flat fossils. *PLoS One* **9**, e86946. (doi:10.1371/journal.pone.0086946)
10. Gueriau P, Mocuta C, Bertrand L. 2015 Cerium anomaly at microscale in fossils. *Analytical Chemistry* **87**, 8827–8836. (doi:10.1021/acs.analchem.5b01820).
11. Gueriau P, Bernard S, Bertrand L. 2016 Synchrotron advanced imaging of paleontological specimens. *Elements* **12**, 45–50. (doi:10.2113/gselements.12.1.45)
12. Schwartz AJ, Kumar M, Adams BL, Field DP (eds.). 2009 Electron backscatter diffraction in materials science. Dordrecht, Springer, 403 p. (doi:10.1007/978-0-387-88136-2)
13. Cusack M. 2016 Biomineral electron backscatter diffraction for palaeontology. *Palaeontology* **59**, 171–179. (doi:10.1111/pala.12222)
14. Päßler JF, Jarochowska E, Bestmann M, Munnecke A. 2018 Distinguishing biologically controlled calcareous biomineralization in fossil organisms using electron backscatter diffraction (EBSD). *Frontiers in Earth Science* **6**, 16. (doi:10.3389/feart.2018.00016)
15. De Nolf W, Dik J, Van der Snickt G, Wallert A, Janssens K. 2011 High energy X-ray powder diffraction for the imaging of (hidden) paintings. *Journal of Analytical Atomic Spectrometry* **26**, 910–916. (doi:10.1039/C0JA00255K)
16. Mürer FK, Sanchez S, Álvarez-Murga M, Di Michiel M, Pfeiffer F, Bech M, Breiby DW. 2018 3D maps of mineral composition and hydroxyapatite orientation in fossil bone samples obtained by X-ray diffraction computed tomography. *Scientific Reports* **8**, 10052. (doi:10.1038/s41598-018-28269-1)

17. Cook PK, Mocuta C, Dufour É, Languille MA, Bertrand L. 2018 Full-section otolith microtexture imaged by local-probe X-ray diffraction. *Journal of Applied Crystallography* **51**, 1182–1196. (doi:10.1107/S1600576718008610)
18. Leclercq N, Berthault J, Langlois F, Le S, Poirier S, Bisou J, Blache F, Medjoubi K, Mocuta C. 2015 Flyscan: a fast and multi-technique data acquisition platform for the SOLEIL beamlines. *ICALEPCS 2015, the 15th International Conference on Accelerator and Large Experimental Control Systems*, 17–23 October 2015, Melbourne, Australia, Abstract No. WEPGF056. (doi:10.18429/JACoW-ICALEPCS2015-WEPGF056)
19. Kirkpatrick P, Baez AV. 1948 Formation of optical images by x-rays. *Journal of the Optical Society of America* **38**, 766–774. (doi:10.1364/JOSA.38.000766)
20. Basolo S, Bérar J-F, Boudet N, Breugnon P, Caillot B, Clemens J-C, Delpierre P, Dinkespiler B, Koudobine I, Meesen C, Menouni M, Mouget C, Pangaud P, Potheau R, Vigeolas E. 2005 XPAD: pixel detector for material sciences. *IEEE Transactions on Nuclear Science* **52**, 1994–1998. (doi:10.1109/TNS.2005.856818)
21. Pangaud P, Basolo S, Boudet N, Bérar J-F, Chantepie B, Clemens J-C, Delpierre P, Dinkespiler B, Medjoubi K, Hustache S, Menouni M, Morel C. 2008, XPAD3-S: A fast hybrid pixel readout chip for X-ray synchrotron facilities. *Nuclear Instruments and Methods in Physics Research A* **591**, 159–162. (doi:10.1016/j.nima.2008.03.047)
22. Medjoubi K, Bucaille T, Hustache S, Bérar J-F, Boudet N, Clemens J-C, Delpierre P, Dinkespiler B. 2010 Detective quantum efficiency, modulation transfer function and energy resolution comparison between CdTe and silicon sensors bump-bonded to XPAD3S. *Journal of synchrotron radiation* **17**, 486–495. (doi:10.1107/S0909049510013257)
23. Le Bourlot C, Landois P, Djaziri S, Renault P-O, Le Bourhis E, Goudeau P, Pinault M,

Mayne-L'Hermite M, Bacroix B, Faurie D, Castelnau O, Launois P, Rouzière S. 2012 Synchrotron X-ray diffraction experiments with a prototype hybrid pixel detector. *Journal of Applied Crystallography* **45**, 38–47. (doi:10.1107/S0021889811049107)

24. Mocuta C, Richard M-I, Fouet J, Stanescu S, Barbier A, Guichet C, Thomas O, Hustache S, Zozulya AV, Thiaudière D. 2013 Fast pole figure acquisition using area detectors at the DiffAbs beamline–Synchrotron SOLEIL. *Journal of applied crystallography* **46**, 1842–1853. (doi:10.1107/S0021889813027453)
25. Charbonnier S. 2009 Un environnement bathyal au Jurassique : le Lagerstätte de La Voulte. *Mémoires du Muséum national d'Histoire naturelle* **199**, 272p.
26. Charbonnier S, Audo D, Caze B, Biot V. 2014 The La Voulte-sur-Rhône Lagerstätte (Middle Jurassic, France). *Comptes Rendus Palevol* **13**, 369–381. (doi:10.1016/j.crpv.2014.03.001)
27. Wilby PR., Briggs DEG., Riou B. 1996 Mineralization of soft-bodied invertebrates in a Jurassic metalliferous deposit. *Geology* **24**, 847–850. (doi: 10.1130/0091-7613(1996)024<0847:MOSBII>2.3.CO;2)
28. Vannier J, Schoenemann B, Gillot T, Charbonnier S, Clarkson E. 2016 Exceptional preservation of eye structure in arthropod visual predators from the Middle Jurassic. *Nature communications* **7**, 10320. (doi:10.1038/ncomms10320)
29. Jauvion C, Bernard S, Gueriau P, Mocuta C, Pont S, Benzerara K, Charbonner S. 2020 Exceptional preservation requires fast biodegradation: thylacocephalan specimens from La Voulte-sur-Rhône (Callovian, Jurassic, France). *Palaeontology* **63**, 395–413. (doi:10.1111/pala.12456)
30. Scherrer P. 1918 Bestimmung der Grösse und der inneren Struktur von Kolloidteilchen

580 mittels Röntgenstrahlen. *Nachrichten von der Gesellschaft der Wissenschaften zu Göttingen,*
581 *Mathematisch-Physikalische Klasse* **26**, 98–100.
582 31. Brito PM, Meunier FJ, Clément G, Geffard-Kuriyama D. 2010 The histological structure of
583 the calcified lung of the fossil coelacanth Axelrodichthys araripensis (Actinistia:
584 Mawsoniidae). *Palaeontology* **53**, 1281–1290. (doi:10.1111/j.1475-4983.2010.01015.x)
585 32. Cupello C, Brito PM, Herbin M, Meunier FJ, Janvier P, Dutel H, Clément G. 2015
586 Allometric growth in the extant coelacanth lung during ontogenetic development. *Nature*
587 *Communications* **6**, 8222. (doi:10.1038/ncomms9222)
588 33. Cupello C, Meunier FJ, Herbin M, Janvier P, Clément G, Brito PM. 2017 The homology and
589 function of the lung plates in extant and fossil coelacanths. *Scientific Reports* **7**, 9244.
590 (doi:10.1038/s41598-017-09327-6)
591 34. Cupello C, Clément G, Brito PM. 2019 Evolution of air breathing and lung distribution
592 among fossil fishes. *In* Johanson Z, Underwood C, Richter M. (eds.), Evolution and
593 Development of Fishes, Cambridge University Press, Cambridge, pp. 252–262.
594 35. Gueriau P, Jauvion C, Mocuta C. 2018 Show me your yttrium, and I will tell you who you
595 are: implications for fossil imaging. *Palaeontology* **61**, 981–990. (doi: 10.1111/pala.12377)
596 36. Clément G. 1999 The actinistian (Sarcopterygii) *Piveteauia madagascarensis* Lehman from
597 the Lower Triassic of Northeastern Madagascar: a redescription on the basis of new
598 material. *Journal of Vertebrate Paleontology* **19**, 234–242.
599 (doi:10.1080/02724634.1999.10011137)
600 37. Martill DM. 1988 Preservation of fish in the Cretaceous Santana formation of Brazil.
601 *Palaeontology* **31**, 1–18.
602 38. Martill DM. 1990 Macromolecular resolution of fossilized muscle tissue from an

elopomorph fish. *Nature* **346**, 171–172. (doi:10.1038/346171a0)

## Figure and table captions

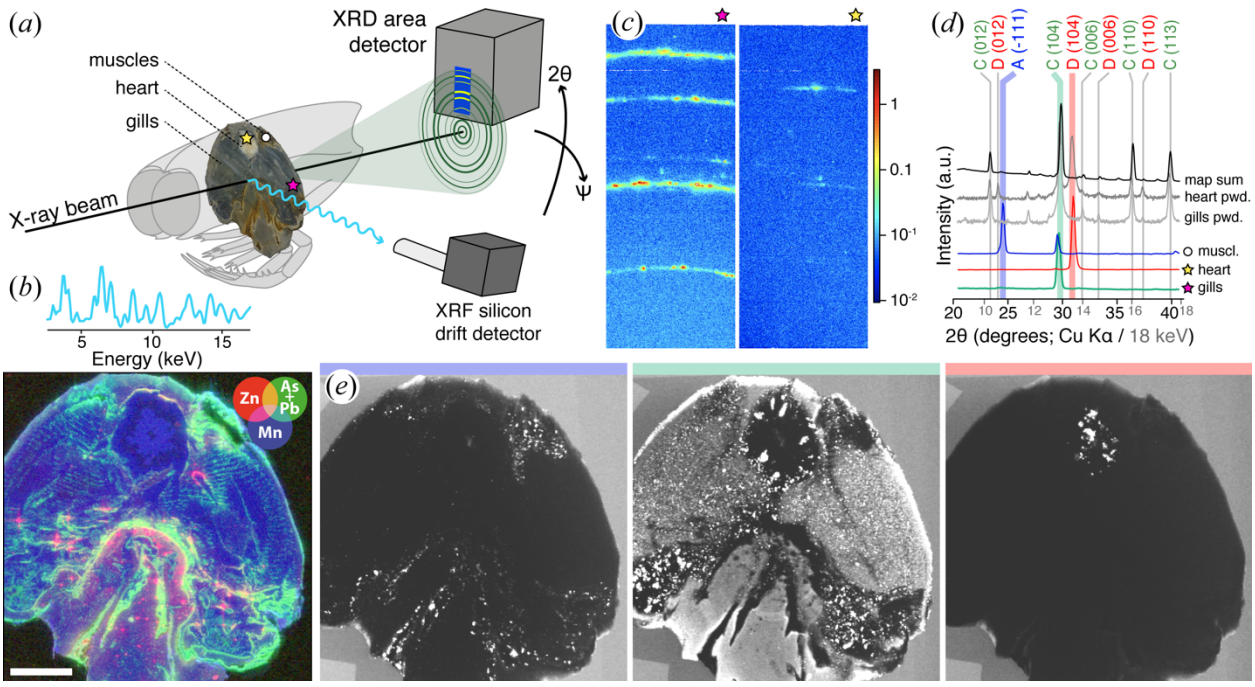


**Figure 1.** SRS-XRFD of a millimetre-thick transversal section of the thylacocephalan arthropod *Dollocaris ingens* (specimen MNHN.F.A66910) from the La-Voulte-sur-Rhône Lagerstätte (Jurassic, France). (*a*) Schematic view of the setup; while laterally scanning the sample with a high energy X-ray beam, an XRD image (blue square) is collected at each pixel using a 2D area detector that intercepts portions of the diffraction rings (red). Simultaneously, an XRF dataset is also acquired in reflection. (*b*) Mean XRF spectrum from a 25-pixel area around the beam location (top), and false colour overlay of zinc (red), arsenic and lead (green) and manganese (blue) distributions (bottom). (*c*) XRD images from pixels in the gills and heart, showing contrasting peaks. (*d*) Mean diffractograms extracted from the XRD map for three different 25-

pixel areas in the gills, heart and muscles (colours; acquired at 18 keV), sum diffractogram from the map (black; acquired at 18 keV), and powder XRD diffractograms obtained from the gills and heart of a more anterior section of the same specimen (grey; acquired at Cu Kα). C, D and A phases are calcite, dolomite and arsenopyrite, respectively. (*e*) XRD intensity maps for 2θ (18 keV) = 10.68° (blue), 13.07° (green) and 13.68° (red), showing different mineralogical contrasts associated to the diffraction peaks highlighted by the corresponding colours in (*d*). Acquisition parameters: 9×11 µm$^2$ (H×V) beam spot size, 75×75 µm$^2$ scan step, 108,900 pixels, 150 (XRF) and 180 (XRD) ms couting times per pixel (total acquisition time 4h51min). Scale bar = 5 mm.

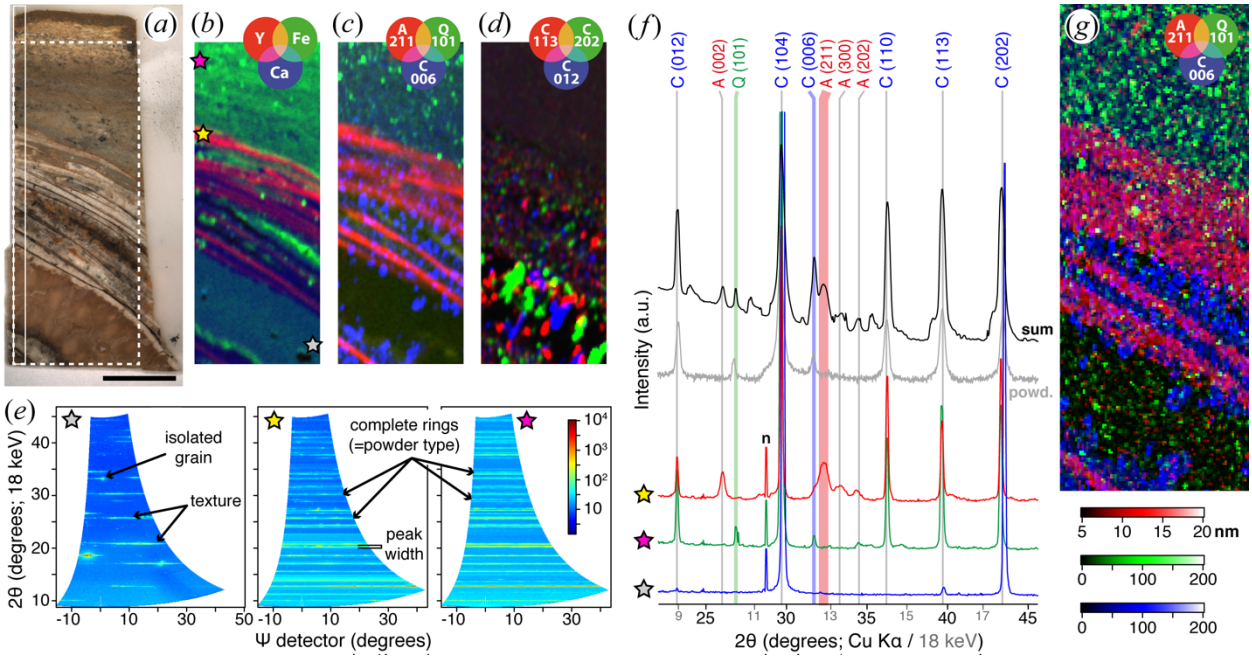


**Figure 2**. SRS-XRFD of a millimetre-thick transversal section through the lung plates of the coelacanth *Axelrodichthys araripensis* (specimen UERJ-PMB 143) from the Santana Formation of the Araripe Basin (Lower Cretaceous, northeastern Brazil). (*a*) Optical photograph of the section. Scale bar = 5 mm. The dotted and solid box areas respectively indicate the area imaged in (*b–d, g*) and the location where the rod-shaped sample in figure 3 was extracted. (*b*) False

colour overlay of yttrium (red), iron (green) and calcium (blue) distributions from XRF. (*c*) False colour overlay of XRD intensity maps for 2θ (18 keV) of apatite (211) (red; 12.70°), quartz (101) (green; 10.40°) and calcite (006) (blue; 12.47°). (*d*) False colour overlay of calcite crystalline planes (113) (red), (202) (green) and (012) (blue) intensity maps showing large intensity fluctuations attributed to texture. (*e*) Combined XPAD images for the 3 areas identified by stars in (*b*) after conversion to (2θ-Ψ) coordinates. (*f*) Mean diffractograms extracted from the XRD map for the three 24-pixel areas identified by stars in (*b*) (colours; acquired at 18 keV), sum diffractogram from the map (black; acquired at 18 keV), and a powder XRD diffractogram obtained from the sedimentary matrix (grey; acquired at Cu Kα). (*g*) Overlay of apatite (211) (red), quartz (101) (green) and calcite (006) (blue) crystallites size. Acquisition parameters: 100×100 $\mu m^2$ (H×V) beam spot size, 100×100 $\mu m^2$ scan step, 25,894 pixels (slightly cropped herein), 45 (XRF) and 37.3 (XRD) ms counting times per pixel (total acquisition time 34min). The XRF and XRD data were acquired simultaneously.

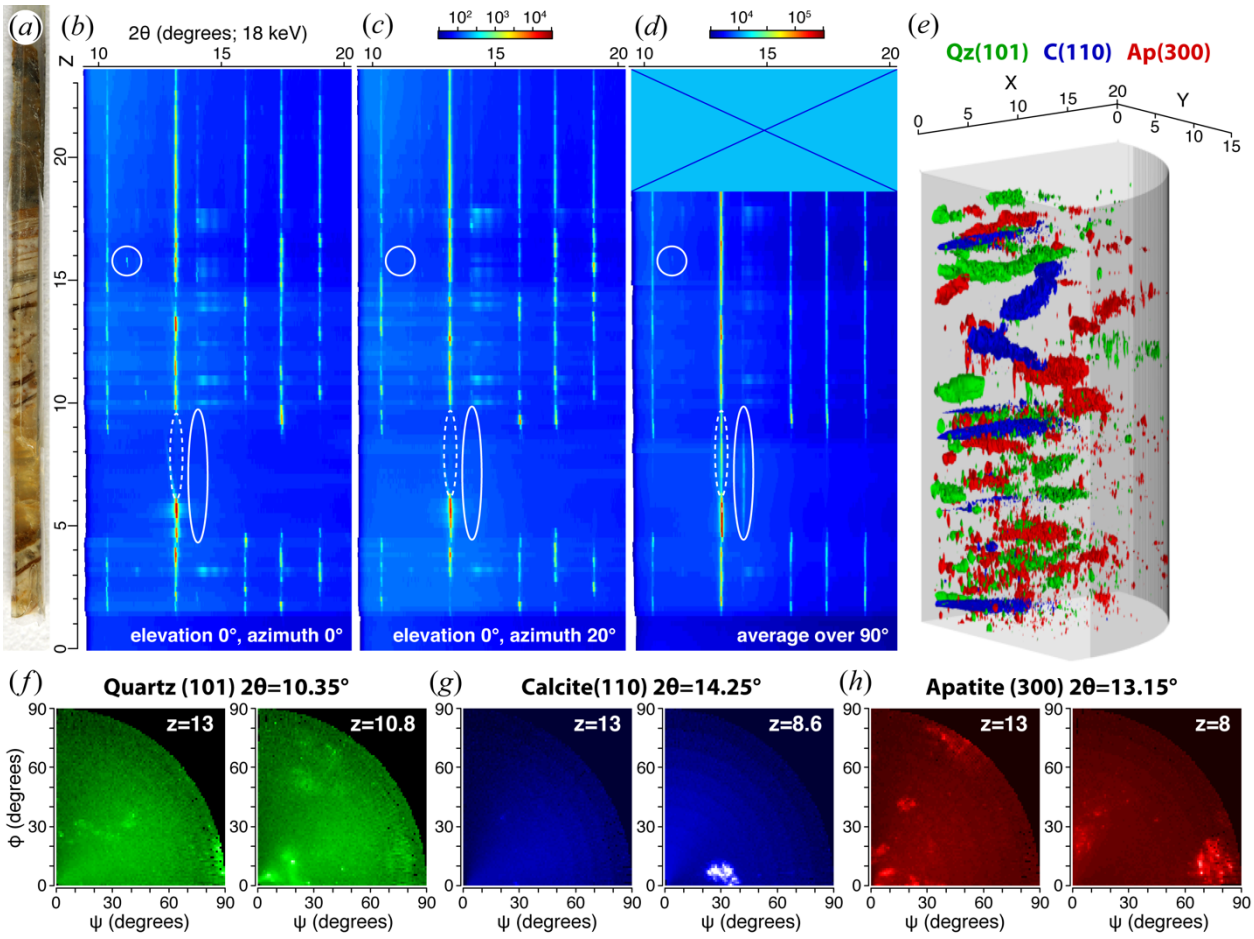


**Figure 3.** Pole figures along a rod-shaped sample extracted from the section through the lung plates of *A. araripensis* (specimen UERJ-PMB 143) shown in figure 2*a*. (*a*) Optical photograph of the sample. (*b,c*) Integrated 2θ intensities along the sample (z-axis), represented as colour map (logarithmic colour scale, from blue to red) for a fixed elevation (0°) and 2 particular azimuths, 0° (*b*) and 20° (*c*). Note the presence of the XRD 'gap' in the sample region z = 5 to 9 mm. (*d*) 2θ intensities averaged over 90° azimuth and elevation ranges. Regions where XRD peaks are different between panels (*b*) and (*c*), or only detected in (*d*), are highlighted by the circles and ellipses respectively. (*e*) 3D representation as iso-surfaces of pole figures along the sample, for particular peaks corresponding to apatite (300, 2θ = 13.15°; red), quartz (101, 2θ = 10.35°; green), and calcite (110, 2θ = 14.25°; blue). (*f-h*) Pole figures (log10 scale, first quadrant only)

for quartz (101) (*f*), calcite (110) (*g*) and apatite (300) (*h*) at z = 13 mm (left) and another z position where a XRD 'slab' can be seen in the 3D view (colour code as in figure 2*g*, using identical amplitudes for each 2θ). All the measurements were performed at an X-ray beam energy of 18 keV.

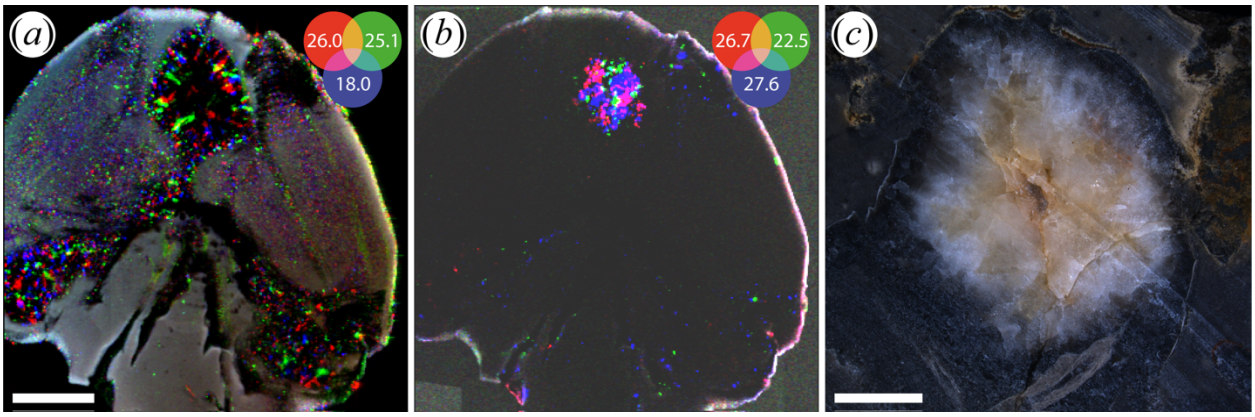


**Figure 4.** Textured mineralisation of the heart in the thylacocephalan arthropod *D. ingens* (specimen MNHN.F.A66910) from the La-Voulte-sur-Rhône Lagerstätte (Jurassic, France). (*a*) False colour overlay of different calcite crystalline planes (for different values of 2θ, in °, at 18 keV). (*b*) False colour overlay of different dolomite crystalline planes (for different values of 2θ, in °, at 18 keV). (*c*) Optical close-up of the heart, showing some of elongated crystal of calcite at the periphery and much poorly organised dolomite at the centre. Acquisition parameters: 9×11 µm$^2$ (H×V) beam spot size, 75×75 µm$^2$ scan step, 108,900 pixels, 180 ms counting time per pixel (total acquisition time 4h51min). Scale bar = 5 mm in (*a,b*) and 1 mm in (*c*).

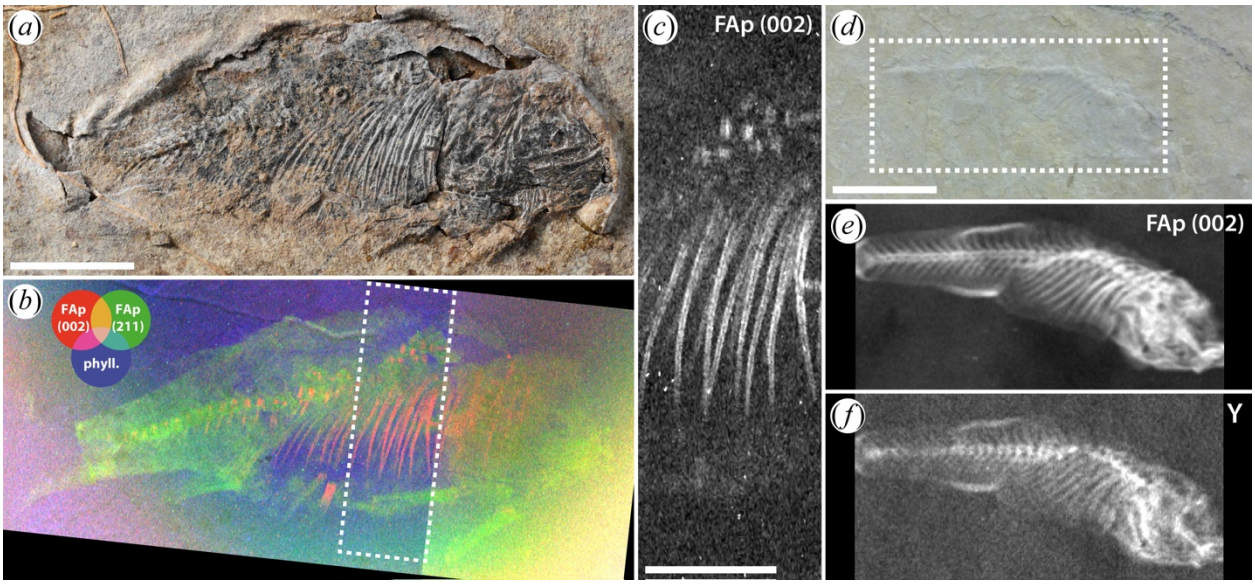


673

674 **Figure 5.** SRS-XRFD imaging of compressed fossil fishes. (*a*) Optical photograph of the
675 osteoglossomorph *Laeliichthys ancestralis* (specimen 099-PV-DZ-UERJ) from the
676 Sanfransiscana Basin, Quiricó Formation (Barremian, southeastern Brazil). (*b*) False colour
677 overlay of XRD intensity maps for fluorapatite (200) (red) and (211) (green), and phyllosilicates
678 (blue). (*c*) XRD intensity map for fluorapatite (002), close-up from the box area in (*b*).
679 Acquisition parameters: 50×50 µm$^2$ (H×V) beam spot size, 35×35 µm$^2$ scan step, 1,182,149
680 pixels (slightly cropped herein), 30 ms counting time per pixel (total acquisition time 24h03min).
681 (*d*) Optical photograph of a hidden cyprinodontiform *Prolebias goreti* (specimen
682 MNHN.F.CRT255) from the Apt-Céreste-Forcalquier Basin (Rupelian, Céreste-Bastide du bois,
683 southern France). (*e*) XRD intensity map for fluorapatite (002). (*f*) Yttrium distribution from
684 XRF. Acquisition parameters: 100×100 µm$^2$ (H×V) beam spot size, 100×100 µm$^2$ scan step,
685 60,750 pixels (cropped herein), 54 (XRF) and 47.8 (XRD) ms counting times per pixel (total
686 acquisition time 1h28min). Scale bar = 1 cm in (*a,b,d–f*) and 5 mm in (*c*).

687 **Table 1.** Age, preservation, sedimentology and nature of the studied samples. Institution abbreviations: MNHN.F, palaeontology
688 collection of the Muséum national d'Histoire naturelle, Paris, France; UERJ, Universidade do Estado do Rio de Janeiro, Rio de
689 Janeiro, Brazil.
690

| species | taxonomy | age | locality | accession no. | preservation and sedimentology | sample nature | figure |
|---|---|---|---|---|---|---|---|
| *Dollocaris ingens* | Arthropoda, ?Crustacea, †Thylacocephala | Callovian (~165 Ma) | La-Voulte-sur-Rhône (France) | MNHN.F.A66910 | carapace in 3D (incl. internal organs and part of appendages) within a metalliferous carbonate concretion | prepared millimeter-thick cross-section | 1*a* |
| *Axelrodichthys araripensis* | Vertebrata, Sarcopterygii, Actinistia | Aptian/Albian (~110 Ma) | Araripe Basin (Brazil) | UERJ-PMB 143 | lung ossified plates and void-infilling in 3D within a carbonate concretion | - prepared millimeter-thick cross-section<br>- prepared 'rod'-shaped sample | 2a<br>3*a* |
| *Laeliichthys ancestralis* | Vertebrata, Actinopterygii, Osteoglossomorpha | Barremian (~125 Ma) | Sanfransiscana Basin (Brazil) | 099-PV-DZ-UERJ | compressed skeleton (incl. scales) in a soft, ferruginous paper shale | unprepared compressed fossil on thin slab | 5*a* |
| *Prolebias goreti* | Vertebrata, Actinopterygii, Cyprinodontiformes | Rupelian (~30 Ma) | Apt-Céreste-Forcalquier Basin (France) | MNHN.F.CRT 255 | compressed skeleton hidden within a fine-grained limestone | unprepared compressed fossil on thin slab | 5*d* |

691